Dielectric Loss Tangent Extraction Using Modal Measurements and 2-D Cross-Sectional Analysis for Multilayer PCBs

Shaohui Yong, *Student Member, IEEE*, Victor Khilkevich, *Member, IEEE*, Yuanzhuo Liu, *Student Member, IEEE*, Han Gao, *Student Member, IEEE*, Scott Hinaga, Soumya De, *Member, IEEE*, Darja Padilla, Douglas Yanagawa, and James Drewniak, *Fellow, IEEE*

***Abstract*—Frequency-dependent electrical properties of dielectric materials are one of the most important factors for high-speed signal integrity design. To accurately characterize material's dielectric loss tangent (tanδ) after multilayer printed circuit board fabrication a novel method was proposed recently to extract tanδ using coupled striplines' measured S-parameters and cross-section geometry. By relating modal attenuation factors to the ratio between the differential and common mode per-unit-length resistances, the surface roughness contribution is eliminated and the contributions of dielectric and conductor loss are separated. Here, we specifically decided to avoid using any physical dielectric model in the extraction algorithm in order to eliminate a need for any *a priori* information about dielectric behavior. Further analysis and improvement of the tanδ extraction approach is presented in this article. To evaluate the accuracy of the extraction, the impact of errors due to de-embedding, vector network analyzer measurement, and two-dimensional solver's calculation are taken into account by a statistical error model. A confidence interval of extracted tanδ is provided. To describe the frequency dependence of tanδ, a two-term Djordjevic model is proposed to fit the extracted tanδ curve, which guarantees causality and gives better agreement with measured insertion loss compared to the traditional Djordjevic model.**

***Index Terms*—Conductor surface roughness, confidence interval, de-embedding method, error analysis, fabricated printed circuit board (PCB), frequency-dependent dielectric behavior, stripline.**

I. Introduction

ADEQUATE wideband characterization of printed circuit board (PCB) dielectric substrates is critical in high-speed signal and power integrity design. Traditional approximations using frequency-independent dielectric constant (ε_r) and loss tangent $(\tan\delta)$ may be applicable for low-speed transmission lines, but do not properly account for the extra attenuation caused by energy consumption due to dielectrics polarization at higher frequencies and cannot model phase-delay responses correctly, producing underestimated dielectric loss and non-causality. Nowadays, as serializer/deserializer channels having pulse rise time reduced to only several pico-seconds, availability of frequency-dependent dielectric material parameters up to 40+ GHz play an important role in predicting signal degradation. Inaccurate frequency-dependence will cause significant uncertainty for modern high-speed PCB design, leading to failure to meet required specifications or costly overdesign.

A traditional dielectric material properties extraction method using a split post dielectric resonator (SPDR) [1]–[3] is widely adopted by material vendors to provide nominal ε_r and $\tan\delta$ values at certain frequency points. A dielectric material sample of the required size and shape should be provided for the resonator measurement. ε_r and $\tan\delta$ are calculated using measured resonance frequency shift and decrease of the Q-factor. However, the SPDR measurement is an inherently narrow-band method. To cover a certain frequency band, multiple SPDRs are needed. Also, the required dielectric sample cannot contain any metallization layers, which often requires the fabrication of dedicated samples with potentially different properties compared to the multilayer PCB fabrication process [4]–[6].

The "Root-Omega" transmission-line-based extraction method [7]–[9] was developed to overcome drawback of the SPDR method. It assumes that the frequency dependencies of conductor (α_C) and dielectric (α_D) attenuation factors obey different laws, approximated by power functions, such that they can be separated from the total attenuation (α_T) directly obtained from measured S-parameters. However, as demonstrated in [10], "Root-Omega" method cannot separate the conductor attenuation factor (α_C) influenced by unknown surface roughness very well. Relatively accurate results can only be achieved for very smooth copper surfaces. Besides that, the power functions adopted to fit attenuation factors do not take into account possible loss dispersion of the dielectric. In addition, the values of ε_r and $\tan\delta$ obtained by the SPDR or "Root-Omega" methods are routinely approximated by using

Manuscript received December 27, 2018; revised April 15, 2019, June 14, 2019, and September 18, 2019; accepted October 17, 2019. Date of publication February 17, 2020; date of current version August 13, 2020. This work was supported in part by the National Science Foundation under Grant IIP-1440110. *(Corresponding author: Shaohui Yong.)*

S. Yong, V. Khilkevich, Y. Liu, and J. Drewniak are with the EMC Laboratory, Missouri University of Science and Technology, Rolla, MO 65401 USA (e-mail: sy2m5@mst.edu; khilkevichv@mst.edu; liuyuanz@mst.edu; drewniak@mst.edu).

H. Gao, S. Hinaga, D. Padilla, and D. Yanagawa are with Cisco Systems, Inc., San Jose, CA 95134 USA (e-mail: hgao2@cisco.com; shinaga@cisco.com; darja@cisco.com; yanagawa@cisco.com).

S. De was with Cisco Systems, Inc., San Jose, CA 95134 USA. He is now with Cruise, San Francisco, CA 94103 USA (e-mail: shomude@gmail.com).

Color versions of one or more of the figures in this article are available online at http://ieeexplore.ieee.org.

Digital Object Identifier 10.1109/TEMC.2019.2949021

a Djordjevic model [11] assuming PCB dielectrics with very low dispersion, which provides causality but may not be able to model extra insertion loss (S_{21}) above tens of gigahertz due to practically constant $\tan\delta$ in the frequency band of interest [11]–[13].

Recently, a new dielectric characterization method using the physics-based principle to exclude the influence of foil surface roughness is proposed in [10]. It does not require any *a priori* assumptions about the $\tan\delta$ frequency-dependent behavior. As a follow-up work on the new method, this paper offers a more comprehensive analysis of the extraction procedure along with the error analysis.

This article is arranged as follows. In Section II, the core algorithm of the extraction method is introduced. Section III investigates the influence of potential inhomogeneity of the PCB dielectric on the extraction performance. In Section IV, analysis on the impact of errors due to de-embedding, vector network analyzer (VNA) measurement, and two-dimensional (2-D) solver on the extracted $\tan\delta$ accuracy is presented. The confidence interval of the extracted $\tan\delta$ curve is calculated. Section V provides a discussion about the frequency behavior of $\tan\delta$. A two-term Djordjevic model is proposed to fit the extraction results within the confidence interval. A comparison between the proposed approach and a conventional one-term Djordjevic model is given.

II. Loss Tangent Extraction Methodology

Before describing the extraction method, we would like to define the necessary parameters. Let us assume a three-conductor transmission line. One of the conductors is treated as a reference, and the nodal voltages are defined as the voltages in two remaining conductors relative to the reference

$$\mathbf{V} = \begin{bmatrix} v_1 \\ v_2 \end{bmatrix}.$$

Similarly, the nodal currents are defined as the currents in the two conductors (the return currents are flowing in the reference conductor):

$$\mathbf{I} = \begin{bmatrix} i_1 \\ i_2 \end{bmatrix}.$$

The nodal parameters ($\mathbf{V}$ and $\mathbf{I}$) can be related to the modal ones ($\mathbf{V}_m$ and $\boldsymbol{I}_m$) through the following transformations [14]:

$$\mathbf{V} = \mathbf{T}_v \begin{bmatrix} v_{m1} \\ v_{m2} \end{bmatrix} = \mathbf{T}_v \mathbf{V}_m$$
$$\mathbf{I} = \mathbf{T}_i \begin{bmatrix} i_{m1} \\ i_{m2} \end{bmatrix} = \mathbf{T}_i \mathbf{I}_m \tag{1}$$

where $\mathbf{T}_v$ and $\mathbf{T}_i$ are transformation matrices. If the matrices are defined as

$$\mathbf{T}_v = \begin{bmatrix} 1 & -0.5 \\ 1 & 0.5 \end{bmatrix}$$
$$\mathbf{T}_i = \begin{bmatrix} 0.5 & -1 \\ 0.5 & 1 \end{bmatrix} \tag{2}$$

the modal parameters will correspond to the common and differential modes

$$\mathbf{V}_m = \begin{bmatrix} v_{cc} \\ v_{dd} \end{bmatrix} = \mathbf{T}_v^{-1}\mathbf{V} = \begin{bmatrix} 0.5\,(v_1 + v_2) \\ v_2 - v_1 \end{bmatrix}$$
$$\mathbf{I}_m = \begin{bmatrix} i_{cc} \\ i_{dd} \end{bmatrix} = \mathbf{T}_i^{-1}\mathbf{I} = \begin{bmatrix} i_1 + i_2 \\ 0.5\,(i_2 - i_1) \end{bmatrix}.$$

The nodal voltages and currents in the transmission lines are described by the telegrapher's equations [15]

$$\frac{d\mathbf{V}}{dz} = -\mathbf{Z}\cdot\mathbf{I}$$
$$\frac{d\mathbf{I}}{dz} = -\mathbf{Y}\cdot\mathbf{V} \tag{3}$$

where $\mathbf{Z} = \mathbf{R} + j\omega\mathbf{L}$ and $\mathbf{Y} = \mathbf{G} + j\omega\mathbf{C}$ are nodal PUL impedance and admittance matrices of the transmission line. Equation (3) can be generalized for modal cases as

$$\frac{d\mathbf{V}_m}{dz} = -\mathbf{Z}_m\cdot\mathbf{I}_m$$
$$\frac{d\mathbf{I}_m}{dz} = -\mathbf{Y}_m\cdot\mathbf{V}_m. \tag{4}$$

By plugging (1) into (3), the equations for the modes can be written as follows:

$$\frac{d\mathbf{V}_m}{dz} = -\mathbf{Z}_m\cdot\mathbf{T}_i^{-1}\mathbf{I} \tag{5}$$
$$\frac{d\mathbf{I}_m}{dz} = -\mathbf{Y}_m\cdot\mathbf{T}_v^{-1}\mathbf{V}. \tag{6}$$

Multiplying both sides of (5) by $\mathbf{T}_v$ and (6) by $\mathbf{T}_i$ gives

$$\frac{d\mathbf{V}}{dz} = -\mathbf{T}_v\,\mathbf{Z}_m\mathbf{T}_i^{-1}\mathbf{I} \tag{7}$$
$$\frac{d\mathbf{I}}{dz} = -\mathbf{T}_i\,\mathbf{Y}_m\mathbf{T}_v^{-1}\mathbf{I}. \tag{8}$$

And finally, by comparing (3) with (7) and (8) the modal PUL matrices are obtained

$$\mathbf{Z}_m = \mathbf{T}_v^{-1}\mathbf{Z}\mathbf{T}_i$$
$$\mathbf{Y}_m = \mathbf{T}_i^{-1}\mathbf{Y}\mathbf{T}_v. \tag{9}$$

It is easy to see that the transformation matrices defined as (2) diagonalize the impedance and admittance matrices (9) such that

$$\mathbf{Z}_m = \mathbf{R}_m + j\omega\mathbf{L}_m = \begin{bmatrix} Z_{cc} & 0 \\ 0 & Z_{dd} \end{bmatrix}$$
$$= \begin{bmatrix} R_{cc} + j\omega L_{cc} & 0 \\ 0 & R_{dd} + j\omega L_{dd} \end{bmatrix}$$
$$\mathbf{Y}_m = \mathbf{G}_m + j\omega\mathbf{C}_m = \begin{bmatrix} Y_{cc} & 0 \\ 0 & Y_{dd} \end{bmatrix}$$
$$= \begin{bmatrix} G_{cc} + j\omega C_{cc} & 0 \\ 0 & G_{dd} + j\omega C_{dd} \end{bmatrix}. \tag{10}$$

The transformation matrices (2) together with (9) will be used henceforth to convert the nodal PUL matrices to the modal ones

(10). The propagation constant for each mode is related to the modal PUL parameters as

$$\gamma_{cc,dd} = \sqrt{(R_{cc,dd} + j\omega L_{cc,dd})\,(G_{cc,dd} + j\omega C_{cc,dd})}. \quad (11)$$

The real part of the propagation constant, i.e., the modal attenuation factor can be approximately (but with a high degree of accuracy for practical low-loss transmission lines with $R \ll \omega L$ and $G \ll \omega C$) calculated as [16]

$$\alpha_{cc,dd} \approx \frac{1}{2}\left(R_{cc,dd}\sqrt{\frac{C_{cc,dd}}{L_{cc,dd}}} + G_{cc,dd}\sqrt{\frac{L_{cc,dd}}{C_{cc,dd}}}\right). \quad (12)$$

Information about the dielectric loss in (12) is contained in the PUL conductance G [see below, (24)], so the extraction of the dielectric loss from the attenuation factors (12) would require to determine all other parameters in the formula. The attenuation factors (α_{cc} or α_{dd}) of striplines can be relatively easily determined in the measurement, and the PUL capacitances and inductances can be calculated if the geometry of the stripline and the permittivity of the dielectric are known. However, it is very difficult to determine the PUL resistance R because it is affected by the surface roughness of the transmission line conductors. Existing roughness models have limited accuracy and rely on numerous roughness parameters that are usually not known and need to be tuned. Thus, the per-unit-length (PUL) resistance of a transmission line (R) can never be calculated accurately. To exclude the impact of foil roughness on the loss tangent extraction accuracy, direct usage of the PUL R of the transmission line should be avoided. The new approach proposed here turns to use a pair of coupled traces allowing to relate the $\tan\delta$ to the ratio of modal PUL resistances (K), which is (as will be shown later) largely independent from foil roughness. Coefficient K is defined here as the ratio between differential and common mode PUL R

$$K = \frac{R_{dd}}{R_{cc}}. \quad (13)$$

Let us analyze the parameter K. For translationally uniform weakly coupled striplines (i.e., in the case when the proximity effect [17]–[19] is negligible), the matrix $\mathbf{R}$ is given as [15]

$$\mathbf{R} = \begin{bmatrix} R_{11} & R_{12} \\ R_{12} & R_{11} \end{bmatrix} = \begin{bmatrix} r_1 + r_0 & r_0 \\ r_0 & r_1 + r_0 \end{bmatrix} \quad (14)$$

where r_0 is the resistance of the ground planes, and r_1 is the resistances of traces (this assumes a symmetrical line). In this case, the modal resistance matrix calculated according to (9) is

$$\mathbf{R}_m = \begin{bmatrix} r_0 + \frac{1}{2}r_1 & 0 \\ 0 & 2r_1 \end{bmatrix} = \begin{bmatrix} R_{cc} & 0 \\ 0 & R_{dd} \end{bmatrix}. \quad (15)$$

Let us assume that the resistances r_0 and r_1 correspond to perfectly smooth conductors. Therefore, the parameter K for a smooth transmission line can be calculated as

$$K_{\text{smooth}} = \frac{R_{dd}}{R_{cc}} = \frac{2r_1}{r_0 + \frac{1}{2}\cdot r_1}. \quad (16)$$

The effect of foil roughness on resistance is usually modeled by applying a correction coefficient to the PUL resistance [20]–[22]. The correction coefficients for the traces K_{Ht} and ground planes K_{Hg} can be added to (16) to obtain the value of K for a rough transmission line as follows

$$K_{\text{rough}} = \frac{R_{dd}}{R_{cc}} = \frac{2r_1 \cdot K_{Ht}}{r_0 \cdot K_{Hg} + \frac{1}{2}\cdot r_1 \cdot K_{Ht}}. \quad (17)$$

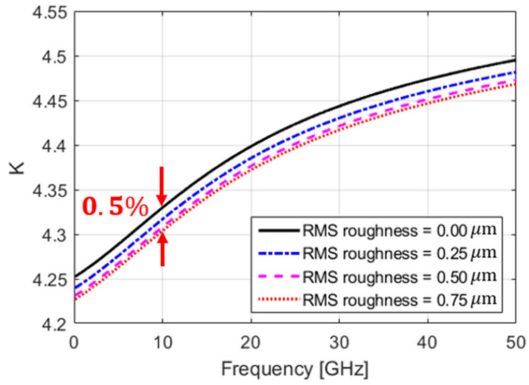

Fig. 1. Resistance ratio K for coupled striplines with different conductor surface roughness (obtained by Ansys Q2D). The cross-section geometry of the coupled striplines is illustrated in Fig. 3. The dielectric constant $\varepsilon_r = 3.4$.

It is obvious that when the roughness of trace and ground conductors is equal, i.e., when $K_{Ht} = K_{Hg}$, the correction coefficients in (17) are eliminated and $K_{\text{smooth}} = K_{\text{rough}}$. Therefore, the ratio K in this case (i.e., when all conductors have equal roughness) is independent of roughness.

It should be noted here that the roughness of traces and ground planes is not always equal. In that case, the ratio K can still be estimated using (17) with the correction coefficients calculated according to Huray (or other) model. However, in this study, the $\tan\delta$ extraction was performed on the PCBs with comparable roughness in ground and trace conductors. Feasibility of extracting $\tan\delta$ in lines with different trace/ground plane roughness requires additional investigation.

The analysis above assumed no proximity effect in the transmission line. In strongly coupled lines, which are ultimately needed for the $\tan\delta$ extraction (see below), the proximity effect cannot be neglected. A general formulation of the resistance matrix with proximity effect in the form similar to (13) is difficult, so to demonstrate the roughness independence of K, a numerical simulation was performed using Ansys Q2D. During the simulation, the roughness of the conductors of the strongly coupled stripline was varied, and the value of K was calculated for each roughness value. As can be seen from Fig. 1, the value of K changes very insignificantly when the foil roughness changes in a wide range – i.e., from a smooth (0.0 μm rms roughness) to a relatively rough case (0.8 μm rms roughness), and the condition $K_{\text{smooth}} = K_{\text{rough}}$ can still be used.

The modal attenuation factors $\alpha_{cc,dd}$ are related to the modal transmission coefficients by a simple formula

$$\alpha_{cc,dd} = \frac{-\ln\left[|S_{cc21,dd21}|\right]}{l} \quad (18)$$

where S_{cc21} and S_{dd21} are the de-embedded modal transmission coefficients (i.e., normalized to the modal characteristic

impedances), and l is the length of the transmission line after de-embedding.

Any suitable de-embedding procedure can be used to obtain the modal transmission coefficients (for example a TRL calibration). In the presented implementation, we used a variant of the 2x thru de-embedding technique known as "eigenvalue de-embedding" [23]–[26]. The choice was made primarily because it is a precise de-embedding technique for translationally uniform transmission lines and uses a minimal number of standards (just two lines of different length). The procedure is designed for single-ended lines; therefore, it is necessary to explain here how it can be applied to coupled striplines. To apply the de-embedding, the VNA is calibrated first to remove all asymmetries between the ports, and hence additional mode conversion. Then the single-ended S-parameters ($\mathbf{S}'$) of the four-port standards are measured and converted to the modal ones ($\mathbf{S}'_M$) by the following transformation:

$$\mathbf{S}'_M = \mathbf{M}\mathbf{S}'\mathbf{M}^{-1} \tag{19}$$

where $\mathbf{M}$ is the transformation matrix (the prime symbols in the formula indicate raw, non-de-embedded S-parameters). To obtain common and differential S-parameters, the transformation matrix is defined as [14] (the definition reflects the port numbering convention)

$$\mathbf{M} = \frac{1}{\sqrt{2}}\begin{bmatrix} 1 & -1 & 0 & 0 \\ 0 & 0 & 1 & -1 \\ 1 & 1 & 0 & 0 \\ 0 & 0 & 1 & 1 \end{bmatrix}. \tag{20}$$

The structure of $\mathbf{S}'_M$, in general, is the following:

$$\mathbf{S}'_{\boldsymbol{M}} = \begin{bmatrix} S'_{dd11} & S'_{dd12} & S'_{\mathrm{dc}11} & S'_{\mathrm{dc}12} \\ S'_{dd21} & S'_{dd22} & S'_{\mathrm{dc}21} & S'_{\mathrm{dc}22} \\ S'_{cd11} & S'_{cd12} & S'_{cc11} & S'_{cc12} \\ S'_{cd21} & S'_{cd22} & S'_{cc21} & S'_{cc22} \end{bmatrix}. \tag{21}$$

Assuming that the transmission line is perfectly symmetrical, i.e., all conversion terms are zero (see Fig. 11 below as a practical illustration of this condition), the modal S-parameter matrix can be separated into two modal submatrices as

$$\mathbf{S}'_{\boldsymbol{M}} = \begin{bmatrix} S'_{dd11} & S'_{dd12} & 0 & 0 \\ S'_{dd21} & S'_{dd22} & 0 & 0 \\ 0 & 0 & S'_{cc11} & S'_{cc12} \\ 0 & 0 & S'_{cc21} & S'_{cc22} \end{bmatrix} = \begin{bmatrix} \mathbf{S}'_{dd} & 0 \\ 0 & \mathbf{S}'_{cc} \end{bmatrix}. \tag{22}$$

Since there is no energy exchange between the modes in (22), they can be treated as separate (uncoupled) transmission lines with S-parameter matrices

$$\mathbf{S}'_{dd} = \begin{bmatrix} S'_{dd11} & S'_{dd12} \\ S'_{dd21} & S'_{dd22} \end{bmatrix} \mathbf{S}'_{cc} = \begin{bmatrix} S'_{cc11} & S'_{cc12} \\ S'_{cc21} & S'_{cc22} \end{bmatrix}. \tag{23}$$

After matrices (23) are calculated (for two standards needed for de-embedding), the eigenvalue de-embedding procedure is applied as described in [23] to obtain de-embedded modal transmission coefficients S_{cc21} and S_{dd21} to be used in (18).

The PUL modal conductances (G) are related to the modal dielectric loss tangents as

$$G_{cc,dd} = \tan\delta_{cc,dd} \cdot \omega \cdot C_{cc,dd}. \tag{24}$$

If the stripline dielectric is uniform (a nonuniform case is discussed in Section III), the common and differential loss tangents are equal, such that $\tan\delta_{cc} = \tan\delta_{dd} = \tan\delta$. Taking this into account and by combining (12), (13), and (24), the following system of equations can be written:

$$\begin{cases} \alpha_{dd} = \frac{1}{2}\left(R_{dd}\sqrt{\frac{C_{dd}}{L_{dd}}} + G_{dd}\sqrt{\frac{L_{dd}}{C_{dd}}}\right) \\ \alpha_{cc} = \frac{1}{2}\left(R_{cc}\sqrt{\frac{C_{cc}}{L_{cc}}} + G_{cc}\sqrt{\frac{L_{cc}}{C_{cc}}}\right) \\ G_{dd} = \omega \cdot C_{dd} \cdot \tan\delta \\ G_{cc} = \omega \cdot C_{cc} \cdot \tan\delta \\ K = \frac{R_{dd}}{R_{cc}} \end{cases}. \tag{25}$$

Finally, by solving (25) with respect to tanδ, the following expression can be obtained [10]:

$$\tan\delta = \frac{2}{\omega}\frac{\alpha_{dd}\sqrt{\frac{C_{cc}}{L_{cc}}} - \alpha_{cc}\sqrt{\frac{C_{dd}}{L_{dd}}} \cdot K}{\sqrt{\frac{C_{cc}}{L_{cc}}} \cdot \sqrt{C_{dd}L_{dd}} - \sqrt{\frac{C_{dd}}{L_{dd}}} \cdot \sqrt{C_{cc}L_{cc}} \cdot K}. \tag{26}$$

This formula relates the dielectric dissipation factor to the modal attenuation factors, modal PUL inductances (L), capacitances (C), and the ratio of modal resistances (K).

The PUL capacitances and inductances, as well as K are calculated using a 2-D cross-sectional solver for a known geometry of the transmission line. The real part of the dielectric permittivity needed to perform the 2-D analysis is extracted from the phase constant of the transmission line, which is calculated using the de-embedded transmission coefficients as follows:

$$\beta = \left|\frac{\arg S_{21}}{l}\right|. \tag{27}$$

The phase constant depends on the PUL capacitance and inductance of a transmission line. Besides the transmission line geometry, the PUL capacitance depends on the permittivity of the medium, while the PUL inductance depends on the permeability. Since the PCB conductors and dielectric materials usually are nonmagnetic, the permeability is known (equal to the permeability of vacuum) and the PUL inductance of the TL can be calculated before the permittivity extraction. The PUL inductance is the superposition of internal inductance due to lossy conductors' skin effect (L_{int}) and external inductance (L_{ext}) and the total phase constant β can be expressed as

$$\beta = \omega\sqrt{LC} = \omega\sqrt{(L_{\mathrm{int}} + L_{\mathrm{ext}}) \cdot C}. \tag{28}$$

By introducing a phase constant depending on the external inductance only (i.e., the phase constant due to the TL dielectric)

$$\beta_{\mathrm{diel}} = \omega\sqrt{L_{\mathrm{ext}} \cdot C} \tag{29}$$

the total phase constant can be rewritten as

$$\beta = \beta_{\mathrm{diel}}\sqrt{\frac{L}{L - L_{\mathrm{int}}}}. \tag{30}$$

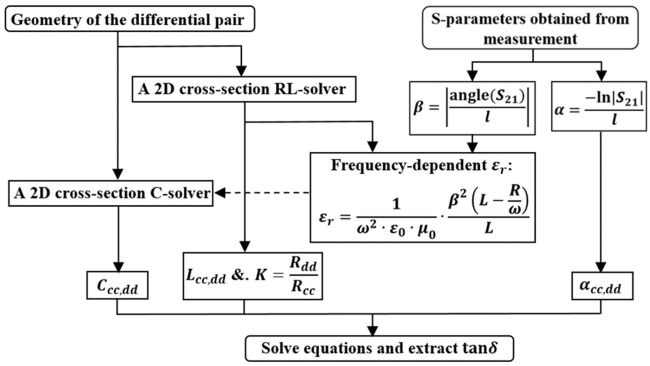

Fig. 2. Flow chart of the proposed $\tan\delta$ extraction method [10].

The constant β_{diel}, in turn, is related to the relative permittivity of the dielectric

$$\beta_{\text{diel}} = \omega\sqrt{\varepsilon_r \varepsilon_0 \mu_0}. \tag{31}$$

By combining (29) with (30) and (31), the relative permittivity can be found as

$$\varepsilon_r = \frac{\beta_{\text{diel}}^2}{\omega^2 \cdot \varepsilon_0 \cdot \mu_0} = \frac{1}{\omega^2 \cdot \varepsilon_0 \cdot \mu_0} \cdot \frac{\beta^2 \left(L - L_{\text{int}}\right)}{L}. \tag{32}$$

According to [22, Ch. 5], the internal inductance L_{int} is related to the PUL resistance of the TL

$$L_{\text{int}} = \frac{R}{\omega}. \tag{33}$$

By combining (32) and (33), the permittivity is finally extracted as

$$\varepsilon_r = \frac{1}{\omega^2 \cdot \varepsilon_0 \cdot \mu_0} \cdot \frac{\beta^2 \left(L - \frac{R}{\omega}\right)}{L} \tag{34}$$

where L and R are calculated by using a 2-D cross-sectional analysis, and β is obtained from the measurement using (27).

The entire dielectric loss tangent extraction procedure is illustrated in the flow chart in Fig. 2.

III. Numerical Validation of the Proposed Extraction Method

To illustrate the feasibility of the proposed method, it is first applied to the simulated transmission line. Two aspects are investigated primarily in this section: the accuracy of ε_r extraction (34) and the influence of possible dielectric inhomogeneity on the $\tan\delta$ extraction accuracy.

A 2-D model of the coupled stripline with the cross-sectional dimensions indicated in Fig. 3 was created. The nodal PUL matrices of the model were calculated by solving a 2-D cross-sectional problem using Ansys Q2D. The PUL matrices are converted to modal form by using (9). The modal attenuation coefficients are calculated according to (18) and the parameter K—according to (13). Finally, the loss tangent is calculated by (26) and compared to the actual value.

To illustrate the extraction accuracy, the model in Fig. 3 was filled with the uniform dielectric material with frequency-independent parameters $\varepsilon_r = 3.4$ and $\tan\delta = 0.003$.

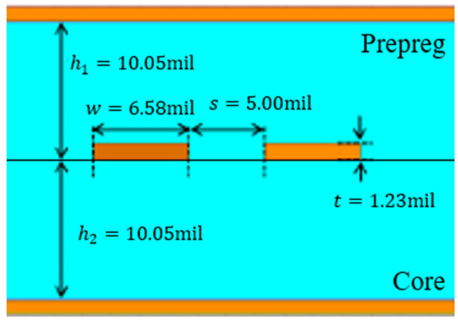

Fig. 3. Cross-section of the stripline model used for loss tangent extraction.

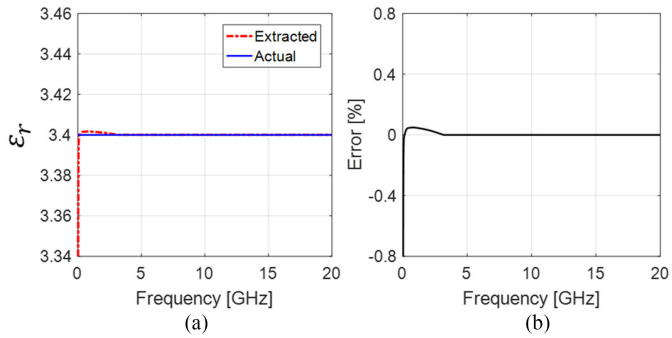

Fig. 4. Extracted dielectric permittivity (a) and the extraction error (b).

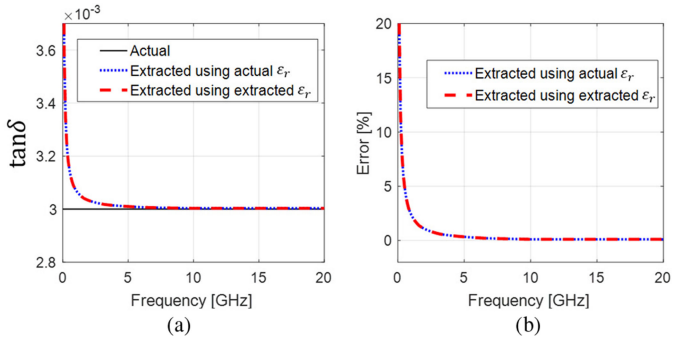

Fig. 5. Extracted loss tangent value using actual and extracted value of permittivity (a) and the corresponding extraction errors (b).

The ε_r extracted using (34) is shown in Fig. 4 along with the actual value as well as the permittivity extraction error. The extraction results are practically overlapping with the actual value, validating the permittivity extraction method.

Next, the loss tangent was extracted according to (26) using actual and extracted [according to (34)] values of the dielectric permittivity. The results are presented in Fig. 5 in comparison to the actual value of loss tangent. The extraction errors are also shown.

As can be seen by comparing curves in Fig. 5(b), the error in permittivity has a minimal impact on the loss tangent extraction. The extracted $\tan\delta$ curve is overlapping with the extraction result obtained using the actual ε_r, which illustrates the insignificance of the observed permittivity extraction error. At the same time both curves diverge from the actual value below 5 GHz,

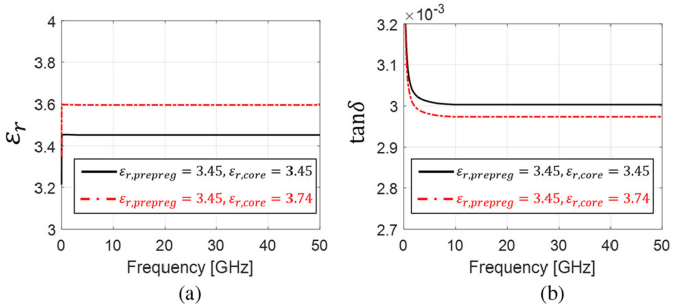

Fig. 6. Extracted ε_r and $\tan\delta$ curves for homogeneous and slightly inhomogeneous cases. For both cases, $\tan\delta_{\text{preg}} = \tan\delta_{\text{core}} = 0.003$; for the homogeneous case (black curve) $\varepsilon_{r,\text{prepreg}} = \varepsilon_{r,\text{core}} = 3.45$; the inhomogeneous case (red curve) is set with 10% differences between $\varepsilon_{r,\text{prepreg}}$ and $\varepsilon_{r,\text{core}}$ ($\varepsilon_{r,\text{prepreg}} = 3.45$, and $\varepsilon_{r,\text{core}} = 3.74$).

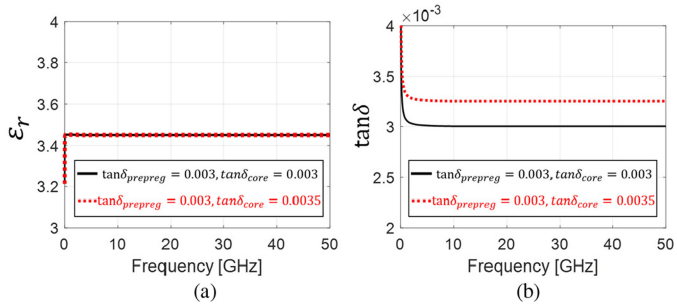

Fig. 7. Extracted ε_r and $\tan\delta$ curves for homogeneous and slightly inhomogeneous cases. For both cases, $\varepsilon_{r,\text{prepreg}} = \varepsilon_{r,\text{core}} = 3.45$; for the homogeneous case (black curve) $\tan\delta_{\text{prepreg}} = \tan\delta_{\text{core}} = 0.003$; the inhomogeneous case (red curve) is set with $\tan\delta_{\text{prepreg}} = 0.003$ and $\tan\delta_{\text{core}} = 0.0035$.

which indicates other sources of errors (besides the error in ε_r) affecting the accuracy of the $\tan\delta$ extraction at low frequencies (see Section V for details and analysis. A two-term Djordjevich model is proposed in Section VI, which essentially extrapolates the permittivity onto the low frequencies).

For striplines in manufactured PCB, the slightly inhomogeneous dielectric material is almost unavoidable because of the fabrication process, glass fiber effect, etc. [4]–[6]. Up to 10% differences in ε_r or $\tan\delta$ between prepreg and core dielectric material may happen in multilayer PCBs [27]. The proposed material extraction method assumes ideally homogeneous dielectric material, which potentially might lead to errors in the extracted $\tan\delta$.

To find the impact of nonideal dielectric material on the extraction procedure, the model in Fig. 3 is filled with inhomogeneous dielectric with the boundary between the regions shown as a horizontal line. The S-parameters are calculated by the 2-D model using different frequency-independent ε_r and $\tan\delta$ for core and prepreg layers, while the extraction is carried out assuming homogeneous dielectric material. The impact of different ε_r in prepreg and core is illustrated in Fig. 6. The extracted ε_r is about 3.6 when $\varepsilon_{r,\text{prepreg}} = 3.45$ and $\varepsilon_{r,\text{core}} = 3.74$, which is approximately the mean value of $\varepsilon_{r,\text{prepreg}}$ and $\varepsilon_{r,\text{core}}$. It is reasonable to treat the extracted ε_r as the effective value. The influence of a 10% difference between $\varepsilon_{r,\text{prepreg}}$ and $\varepsilon_{r,\text{core}}$ on the extracted $\tan\delta$ is illustrated in Fig. 6(b). The value of extracted $\tan\delta$ is less than 1% off from the actual value of the $\tan\delta$, which illustrates low sensitivity of the proposed extraction method to the differences in the dielectric constant of PCB layers.

The situation is different when layers have different $\tan\delta$ values. To illustrate this, the ε_r of both layers was set to 3.45, while the $\tan\delta$ values were different: $\tan\delta_{\text{prepreg}} = 0.003$ and $\tan\delta_{\text{core}} = 0.0035$. As Fig. 7(a) shows, the impact of the $\tan\delta$ difference on the extracted ε_r is negligible. However, it is not the case for $\tan\delta$. As Fig. 7(b) shows, the extracted value of $\tan\delta$ is very close to the mean value of prepreg and core $\tan\delta$, which will be very close to the effective value of $\tan\delta$ for transmission lines with an equal thickness of dielectric layers.

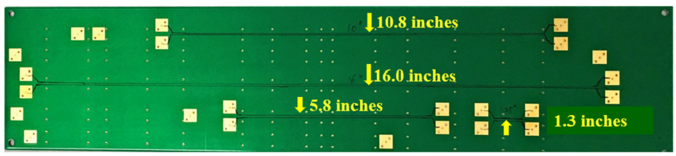

Fig. 8. Testing board with several coupled striplines of different length.

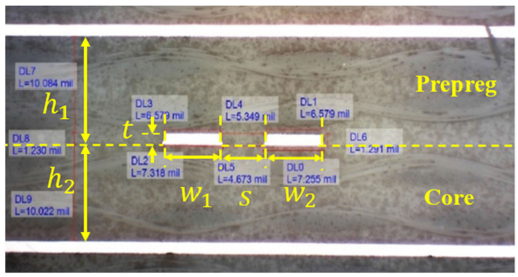

Fig. 9. Cross-section of the coupled striplines. The trace width ($W_1 \approx W_2$) is 6.58 mil; edge-to-edge spacing (s) is 5.30 mil; dielectric height ($h_1 \approx h_2$) is 10.05 mil; trace thickness (t) is 1.23 mil. The yellow dashed line illustrates the boundary between prepreg and core.

The results presented above demonstrate that the proposed extraction method is relatively robust with respect to slight dielectric inhomogeneities in the striplines.

IV. Loss Tangent Extraction Using Measured Data

To test the proposed method in the experiment, a testing vehicle containing multiple differential lines was fabricated (see Fig. 8). The cross-section geometry of the coupled lines is presented in Fig. 9. Two of the lines (1.3 and 15.8 in, with the corresponding de-embedded length of 14.5 in) were used for x2thru measurements. The roughness of ground planes and traces is comparable (the corresponding profiles are given in Fig. 10). An example of raw and de-embedded S-parameters for the 15.8-in transmission line are given in Figs. 11 and 12. The modal PUL parameters along with the parameter K calculated using the geometry information in Fig. 9 in Q2D are shown in Fig. 13. The extracted ε_r and $\tan\delta$ are shown in Fig. 14. The reference $\tan\delta$ value provided by the laminate material maker

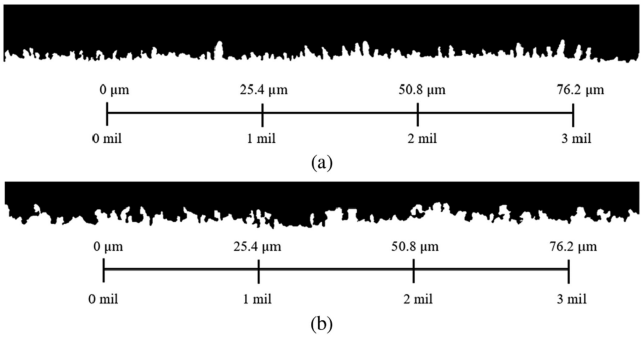

Fig. 10. Profiles of ground (a) and signal (b) conductors obtained using optical microscopy. The rms roughness levels obtained with roughness profile extraction tool [28] is 0.47 μm for ground and 0.41 μm for signal conductors, respectively.

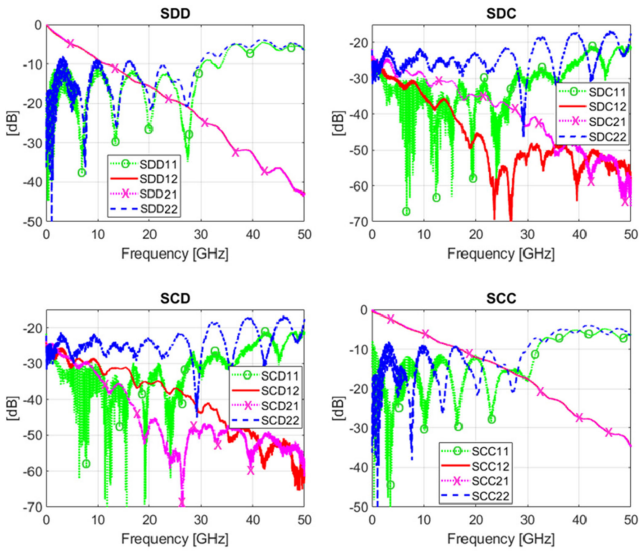

Fig. 11. Raw modal S-parameters for the 15.8-in differential transmission line.

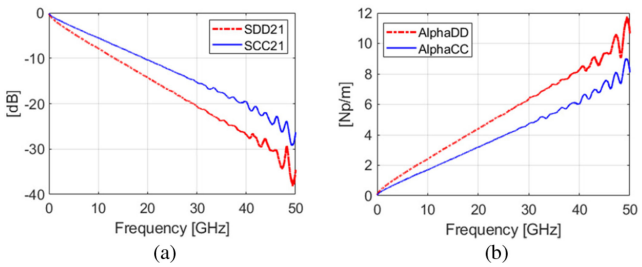

Fig. 12. De-embedded modal insertion loss (a) and attenuation factor (b) for the 15.8-in line using the 1.3-in line as a thru.

is about 0.003 at 10 GHz, which is very close to the extraction result.

V. Error Model for the Loss Tangent Extraction Method

As can be seen in Fig. 14, the extracted loss tangent curve is relatively "clean" from 5 to 30 GHz, however variations below and above this interval are significant. Obviously, the

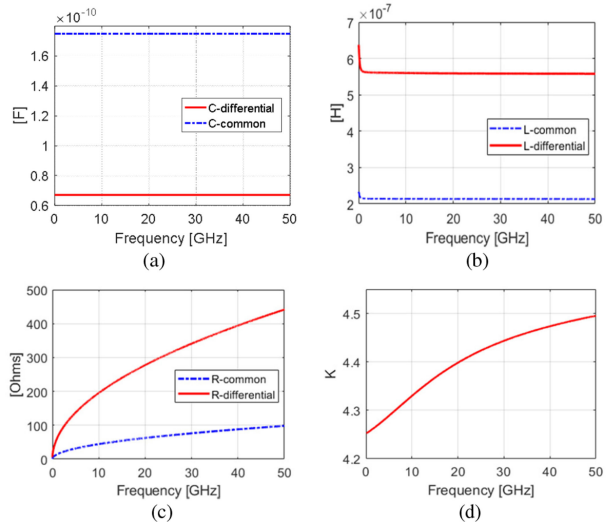

Fig. 13. Components of the modal C (a) calculated using extracted ε_r, (b) L, (c) R matrices calculated using (5) and (d) the parameter K calculated using (9). The cross-sectional analysis is performed using Ansys Q2D.

behavior below 5 and above 30 GHz is nonphysical and requires explanation. The most obvious reason for this is simulation/measurement inaccuracies and the sensitivity of the extraction formula (26) to them (as can be seen from Section III, inaccuracies caused by approximations in the extraction process are of much lower level).

The proposed $\tan\delta$ extraction method requires several groups of data

1) raw S-parameters obtained by the VNA measurement;
2) de-embedded S-parameters to obtain attenuation factors;
3) PUL inductance, capacitance, and K calculated by a 2-D cross-sectional solver.

Therefore, three sources of errors can be identified: measurement errors, de-embedding errors, and simulation errors. Not all of these errors can be estimated accurately. For example, the simulation errors are especially difficult to determine directly because the actual PUL parameters of the transmission lines are not accessible. Besides this, the systematic (i.e., nonrandom) components of errors are difficult to determine because of the lack of references (i.e., an independent measurement method). Because of these limitations, the error analysis listed below cannot be called comprehensive, but we believe that it is still useful because it allows us to explain peculiarities of the extracted loss tangent curves and determine frequency range where the extracted data are the most accurate.

A. Simulation Errors

The resistance ratio K can be calculated correctly only if the metal conductors are meshed (as opposed to the boundary conditions on the surface) as demonstrated in [10], and the error strongly depends on the mesh density. Accuracy of the other simulated parameters (L and C) is also strongly dependent on the mesh. Therefore, the accuracy of the simulated parameters is estimated by mesh refinement [29].

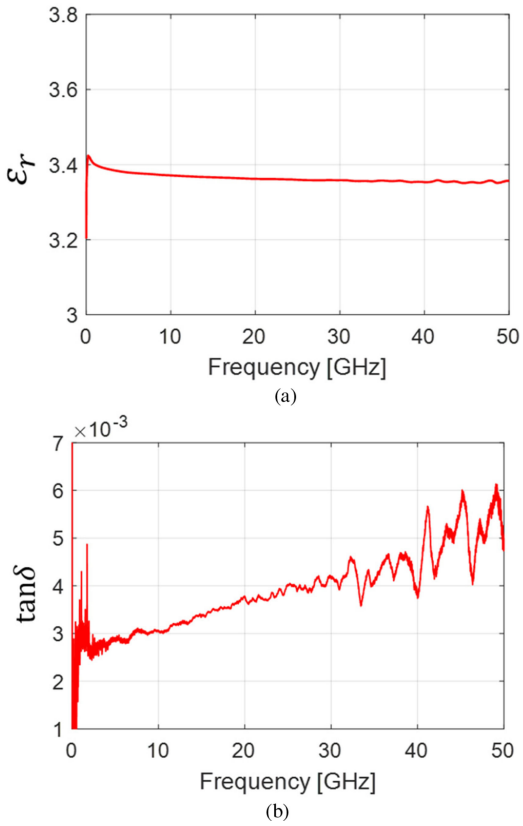

Fig. 14. Extracted ε_r (a) and $\tan\delta$ (b) curves obtained by using the proposed method.

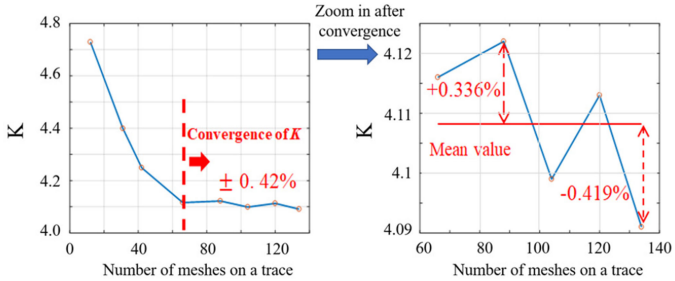

Fig. 15. Simulation error of the parameter *K* estimated by mesh refinement.

To achieve this, the mesh count is gradually increased and for each mesh the parameters K, L, and C are calculated. As the mesh density increases the parameters converge to certain values. The simulation error is, therefore, estimated using the variations of converged *K*, *L*, and *C* over several last iterations. An example of convergence curves at 5 GHz for the geometry in Fig. 9 is shown in Figs. 15 and 16. The variations of parameters were estimated as $\Delta K = \pm 0.4\%$, $\Delta L = \pm 0.01\%$, and $\Delta C = \pm 0.01\%$.

The influence of the simulation parameter accuracy on the accuracy of the extracted $\tan\delta$ was estimated numerically. To achieve this, a statistical model for the simulated parameters is created by assuming Gaussian distribution with the mean value equal to the simulated value at the last mesh refinement

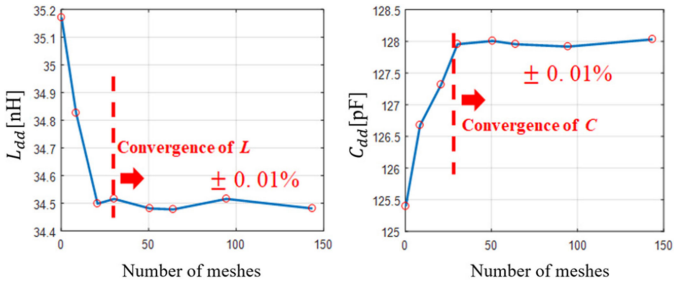

Fig. 16. Simulation error of K, L, and C estimated by mesh refinement.

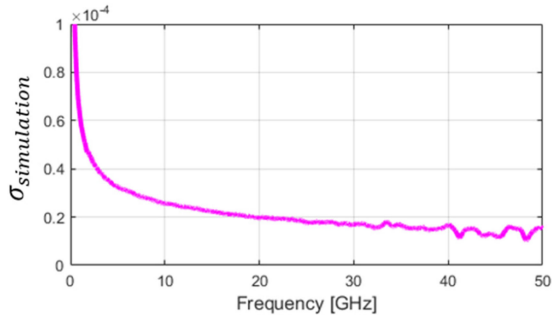

Fig. 17. Estimated standard deviation of extracted $\tan\delta$ calculated using *K*, *L*, and *C* subjected to Gaussian distribution. The actual $\tan\delta$ value is 3×10^{-3} at 10 GHz.

step and the standard deviation equal to 1/3 of the variations determined above (such that the variations are within 99% confidence interval). Five thousand random samples of the parameters were calculated, representing 5000 random combinations of the simulation parameters. For each of the combinations, the value of $\tan\delta$ was calculated according to (26) and its standard deviation at each frequency was calculated (see Fig. 17).

As can be seen, the extracted $\tan\delta$ errors are relatively large at low frequencies, and then gradually decrease with the increase of frequency. High error at low frequencies is due to poor conditioning of the system of (12) (indeed, at dc the difference between α_{dd} and α_{cc} is very small). As the frequency increases, the conditioning of (12) improves, while the errors of the simulated parameters remain constant, leading to a decrease of the $\tan\delta$ error.

B. Error Due to De-Embedding

All de-embedding methods require identical fixtures in total and thru lines (Fixture 1A = Fixture 2A; Fixture 1B = Fixture 2B, as shown in Fig. 18). For the "eigenvalue" de-embedding (also known as, "Delta-L") [23]–[26] method used in this study, the symmetric design in fixtures for both total and thru lines (Fixture 1A = Fixture 1B = Fixture 2A = Fixture 2B) is also required.

However, in reality, the transitions from coaxial to stripline medium cannot be made perfectly identical due to geometrical variations and variability in the connector-pad transitions (this is evident in the TDR plots below). For the sake of the error analysis, we assume that the source of de-embedding inaccuracies

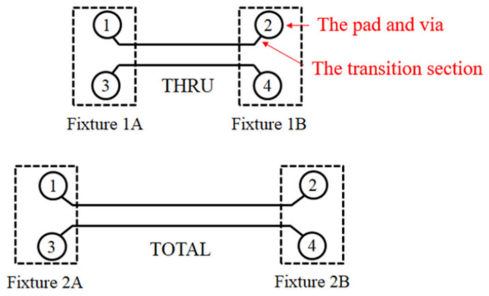

Fig. 18. Total and thru fixture definition. The fixture is composed of the connector, pad, plated-thru hole, via and transition section, etc. Manufacturing variation will cause differences between fixtures, such as the length of back-drilled stubs.

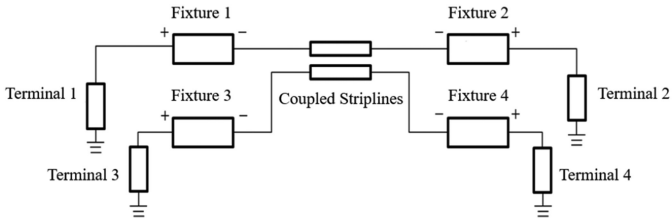

Fig. 19. Overview of the Keysight ADS de-embedding model.

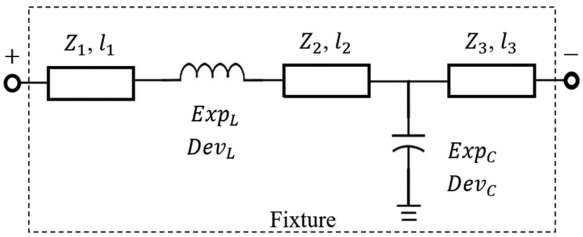

Fig. 20. Circuit fixture model (fixtures 1–4). The expectation and the standard deviation of the inductor and capacitor are tuned to achieve agreement with the measured TDR ($\mathrm{Exp}_L = 1.75 \times 10^{-11}\ H;\ \mathrm{Dev}_L = 40\%;\ \mathrm{Exp}_C = 4.8 \times 10^{-14}\ F;\ \mathrm{Dev}_C = 11\%$).

is the variations in the transitions from the coaxial cable to the differential stripline [30], violating identical and symmetrical assumptions formulated above.

The error estimation strategy, therefore, is to estimate the variations of the transitions and then numerically propagate them through the de-embedding and extraction calculations and finally estimate the error of the extracted loss tangent.

To achieve this, a circuit model of the transmission lines with fixtures (transitions) was created (see Figs. 19 and 20). Each fixture is modeled by an excessive inductance and capacitance along with short portions of transmission lines. The values of excessive capacitance and inductance are assumed to be normally distributed. The mean value and standard deviation of the capacitance and inductance are tuned to match the shape and the spread of the measured TDR response of the transmission lines as illustrated in Fig. 21 (since two differential lines are used for each measurement, a total of eight TDR curves are used to estimate the statistical parameters of the fixture models). Due to

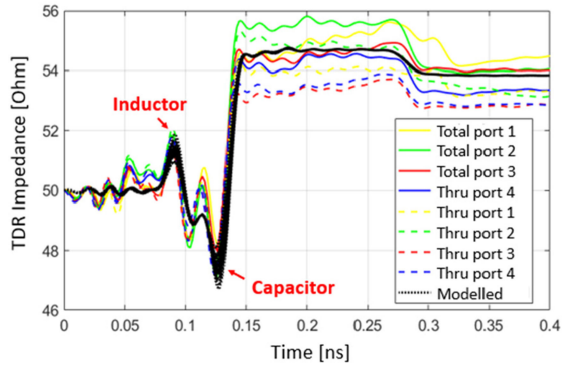

Fig. 21. Measured and modeled fixture TDR responses. Modeled response contains multiple curves due to the model parameter variations.

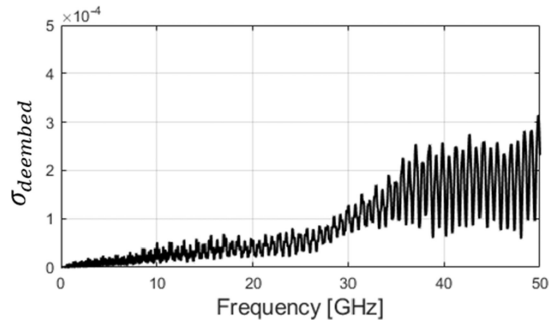

Fig. 22. Standard deviation of extracted $\tan\delta$ calculated using 1000 sets of de-embedded S-parameters. The Thru line length is 1.3 in, and the total line length is 16 in. The actual $\tan\delta$ value is 3×10^{-3} at 10 GHz.

the relatively low number of samples (eight curves), the statistics cannot be determined exactly, but a rough estimation still can be made.

After the fixture model is created, a Monte-Carlo simulation is performed (with random values of excessive inductances and capacitances in all transitions) and 1000 random combinations of the thru and total S-parameters are created for de-embedding. The 1000 extracted $\tan\delta$ curves are then used to estimate the standard deviation of the $\tan\delta$.

The $\tan\delta$ standard deviation curve ($\sigma_{\mathrm{deembed}}$) is presented in Fig. 22. As can be seen from the plot, the de-embedding error, in general, increases with frequency due to the increase of the fixture reflections (and hence increased influence of their variability); however, at some frequencies where the de-embedding equation is relatively poorly conditioned, the sensitivity to errors is higher. In general, the error curve contains a periodic pattern, the periodicity of which depends on the electrical lengths of the thru and total standards.

C. VNA Measurement Error

The S-parameters measurement is performed using Keysight N5244A 4-PORT PNA-X Network Analyzer. The VNA calibration is performed using an electronic calibration kit N4692. With proper choice of averaging factor and intermediate frequency bandwidth, the VNA measurement noise can be reduced

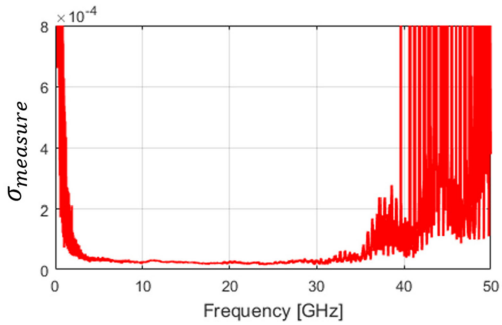

Fig. 23. Standard deviation of the extracted $\tan\delta$ calculated using 400 sets of VNA measured S-parameters. The actual $\tan\delta$ value is 3×10^{-3} at 10 GHz.

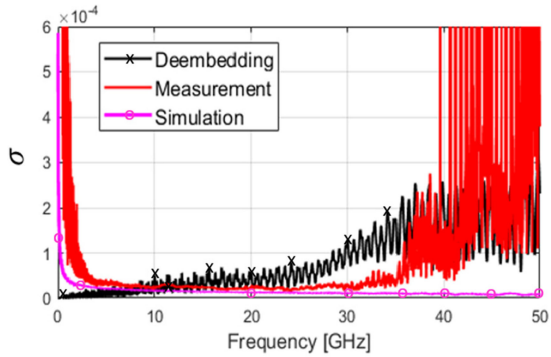

Fig. 24. Contributions to the standard deviation of the extracted $\tan\delta$ due to the measurement error (σ_{meas}), de-embedding error $(\sigma_{\text{deembed}})$, and simulation error (σ_{simu}). The Thru line length is 1.3 in, and the total line length is 16 in. The actual $\tan\delta$ value is about 3×10^{-3} at 10 GHz.

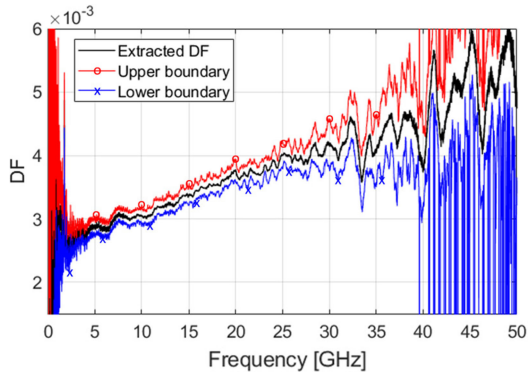

Fig. 25. Thru line length is 1.3 in, and the total line length is 16 in. The extracted $\tan\delta$ curve and confidence intervals are calculated.

to quite low levels. However, frequency-dependent measurement error is still unavoidable [31]. To estimate the impact of frequency-dependent VNA measurement error to the $\tan\delta$ extraction method, a statistical analysis of the measurement data is performed.

The following procedure was used to estimate the measurement errors. After the VNA calibration, several tens of thru and total S-parameters are saved (without disconnecting the cables in each case). After that, several hundreds of thru/total S-parameter combinations are created for de-embedding and for each of them the value of $\tan\delta$ is calculated. The standard deviation $(\sigma_{\text{measure}})$ of extracted $\tan\delta$ curve is estimated (see Fig. 23). Since the fixtures remain the same during the measurements and fixed values of the simulated parameters (*L*, *C*, and *K*) are used for extraction, the variability in the extracted loss tangent is due to the measurement error only. Fig. 23 shows that large VNA measurement error occurs at relatively low frequency (below 1 GHz), and it decreases as frequency goes up. The minimum error appears around several gigahertz and remains low up to 35 GHz; after that it starts to grow rapidly. High error level at low frequencies can be explained by poor conditioning of the system of (12) (the values of α_{cc} and α_{dd} become very close to each other). At high frequencies, the contribution of the measurement noise increases (simply because the transmission coefficients decrease in absolute value and become comparable to noise).

D. Confidence Interval of Extracted Loss Tangent

The contributions of all three factors (simulation error, de-embedding error, VNA measurement error) estimated for the test vehicle in Fig. 8 are compared in Fig. 24. As can be seen, below 4 GHz the measurement and simulation errors dominate, then from 10 up to 40 GHz the de-embedding error is the dominating factor, and above 40 GHz, the measurement and de-embedding errors become comparable.

Assuming that the different error sources are independent to each other, the total standard deviation of extracted $\tan\delta$ is calculated using a property of a linear combination of independent random variables as

$$\sigma_{\text{total}} = \sqrt{(\sigma_{\text{deembed}})^2 + (\sigma_{\text{measure}})^2 + (\sigma_{\text{simu}})^2}. \quad (35)$$

Finally, the $\tan\delta$ can be modeled as a Gaussian variable

$$\tan\delta - \text{Gaussian}\left(\tan\delta_{\text{nominal}}, \sigma_{\text{total}}\right) \quad (36)$$

where $\tan\delta_{\text{nominal}}$ is the extracted value of the loss tangent. The upper $(\tan\delta_{\text{upper}})$ and lower $(\tan\delta_{\text{lower}})$ bounds of extracted $\tan\delta$ confidence interval are defined using 99% confidence level with $(3 \cdot \sigma_{\text{total}})$ as

$$\tan\delta_{\text{upper}} = \tan\delta_{\text{nomianl}} + 3 \cdot \sigma_{\text{total}} \quad (37)$$

$$\tan\delta_{\text{lower}} = \tan\delta_{\text{nomianl}} - 3 \cdot \sigma_{\text{total}}. \quad (38)$$

The extracted curve along with the confidence intervals is presented in Fig. 25, and the corresponding confidence interval expressed in percent—in Fig. 26. As can be seen, in the interval from 3 to 30 GHz the extracted $\tan\delta$ error (99% confidence) does not exceed 10%, and on the interval from 5 to 20 GHz it is less than 6%.

As was said above, presented error analysis is not complete and probably gives a conservative estimate of the extraction accuracy. However, it explains the unphysical behavior of the extracted curve below 3 GHz [high sensitivity to errors due to poor conditioning of (12)] and variations above 30 GHz (lack of de-embedding accuracy and influence of the measurement noise).

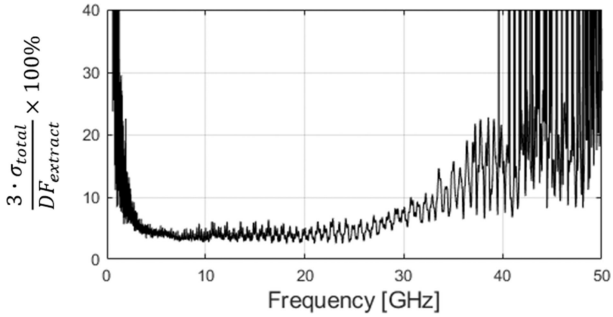

Fig. 26. Estimated extraction error percentage defined as 99% confidence.

VI. Causal Model for Dielectrics With Frequency-Dependent Loss

In Section V, the confidence interval of extracted $\tan\delta$ is calculated. Any curve within the confidence interval (or within the envelopes of the confidence interval as a worst-case estimate) may be a potential candidate for the final output extraction result. Of course, an infinite number of curves satisfy this condition, but based on an *a priori* knowledge about the behavior of typical PCB dielectric materials, the class of possible approximations can be limited to slowly changing (i.e., "smooth") and monotonic curves. Another important consideration is the causality of the selected approximation which would allow using the model for time-domain simulations.

A. Existing Dielectric Models

There are a number of approaches to dielectric modeling that can produce smooth casual responses. One of the most widely used of them is a Djordjevic model [11]. The complex dielectric constant according to the model is calculated as

$$\varepsilon' = \varepsilon'_{\infty} + \frac{\Delta\varepsilon'}{m_2 - m_1} \cdot \frac{\ln\left(\frac{\omega_2}{\omega}\right)}{\ln(10)} \tag{39}$$

$$\varepsilon'' = \varepsilon' \cdot \tan\delta = \frac{\Delta\varepsilon'}{m_2 - m_1} \cdot \frac{-\frac{\pi}{2}}{\ln(10)} \tag{40}$$

where ε'_{∞} is the value of dielectric constant at the infinite frequency, and $\Delta\varepsilon'$ is the difference between the dielectric constant at dc and infinity.

Selection of numbers m_1 and m_2 determines the frequency range from $2\pi f_1 = 10^{m_1}$ to $2\pi f_2 = 10^{m_2}$ with very weak frequency dependency of ε. In practice, the lower frequency is set to the kHz, and the higher frequency to the THz ranges to model weakly dispersive PCB materials.

However, this low-dispersive assumption leads to a practically frequency-independent $\tan\delta$ of the model in the range $f_1 - f_2$, and does not allow modeling the extracted curves similar to one in Fig. 14(b). Moving the lower frequency f_1 into the working frequency range (i.e., from kHz to GHz frequency) does allow to model the loss dispersion but at an inevitable cost of introducing the strongly frequency-dependent dielectric constant.

When the Djordjevic model is used on practice, the loss dispersion is typically ignored and the Djordjevic model with very weakly dispersive ε is created by picking a single value at a certain frequency such as an example in Fig. 27 demonstrates (here, the value at 5 GHz was selected). For extracted $\tan\delta$ such an approach will, of course, lead to underestimation of transmission line loss at higher frequencies.

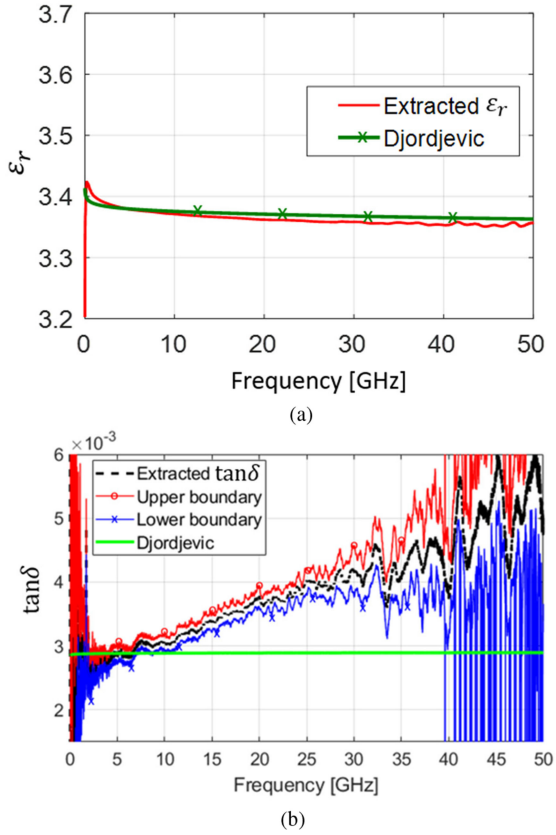

Fig. 27. (a) Etraction results and fitted ε_r; (b) $\tan\delta$ calculated using the extracted ε_r, and the Djordjevic model result.

An alternative to the Djordjevic model is to use a multiterm Debye or Lorenz approximation (an example of a double-term Debye model is presented in [32]). While these approximations can be used on practice, the most important drawback associated with this approach is a need to have multiple terms in approximations for wide frequency ranges (from hundreds of MHz to tens of GHz), leading to large number of parameters to be determined.

Here we would like to propose an extension of the Djordjevic model which allows to produce wideband responses (with practically unlimited frequency bounds) having a frequency-dependent loss using just four parameters.

B. Djordjevic Model With Two Dispersive Terms

As an improvement allowing to model frequency-dependent dielectrics, we propose to add a second Djordjevic term to the dielectric model such that the permittivity of the dielectric is represented as

$$\varepsilon_{\text{tot}} = \varepsilon_{d1} + \varepsilon_{d2} \tag{41}$$

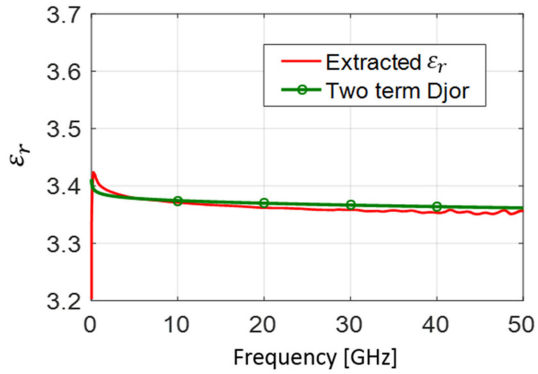

(a)

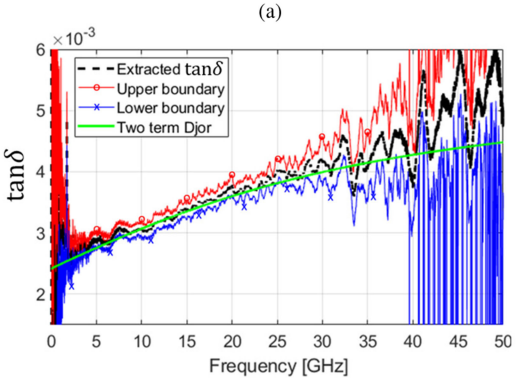

(b)

Fig. 28. (a) Extraction results and fitted ε_r; (b) $\tan\delta$ calculated using the extracted ε_r, and the two-term Djordjevic model result.

TABLE I
TWO-TERM DJORDJEVIC MODEL

	f_1	f_2	m_1	m_2	$\Delta\varepsilon'$	ε'_∞
ε_{d1}	1 kHz	10 THz	3.80	13.80	0.12	3.21
ε_{d2}	30 GHz	10 THz	11.28	13.80	0.04	0.08

where both terms ε_{d1} and ε_{d2} are described by (39) and (40), but have different parameters. The term ε_{d1} is the traditional Djordjevic term with low dispersion in the frequency range of interest, and term ε_{d2} has the frequency f_1 in the GHz frequency range, low dielectric constant (which is fixed and is not a model parameter), and high loss.

The parameters of the model are therefore

1) 1) ε'_∞ for the ε_{d1};
2) 2) $\Delta\varepsilon'$ for the ε_{d1};
3) frequency f_1 for ε_{d2};
4) 4) ε'_∞ or $\Delta\varepsilon'$ for ε_{d2}.

The parameters are tuned (or optimized) to produce the curve that satisfies the confidence interval of the extracted $\tan\delta$ (in the sense defined above) and at the same time approximates the real part of permittivity. An example of approximation is presented in Fig. 28. The approximation parameters are listed in Table I. As can be seen by combining two Djordjevic, it is possible to model frequency-dependent dielectric loss with loss dispersion in the dielectric constant in a very wide frequency range, producing strictly monotonic curves (including all derivatives) with just four parameters.

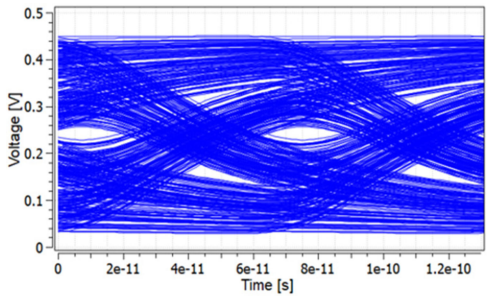

Fig. 29. Eye diagram of the measurement data. The rise/fall time is set to 5 ps, and data rate is 15 Gbps.

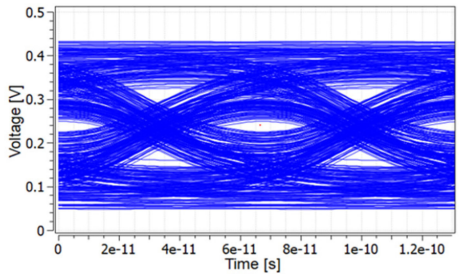

Fig. 30. Modeled eye diagram of the two-term Djordjevic model.

C. Time-Domain Validation of the Proposed Model

The proposed dielectric model (see Fig. 28) was validated by calculating eye-diagrams of the differential channels formed by a 30-in transmission line. The dielectric was modeled by the two-term Djordjevic model as described above and the conductor surface roughness was modeled using the Huray model. The Huray model had the following parameters: rms roughness $h_{\rm rms} = 0.43$ μm, ball size $a_{\rm ball} = 0.63$ μm, number of balls $N_{\rm ball} = 25$, and the tile area $A_{\rm tile} = 90$ μm^2. The parameters for the roughness model were determined empirically for profiles in Fig. 10.

For comparison, the models with a popular one-term Djordjevic models (i.e., practically frequency-independent loss) were also created. The eye diagrams for all models in the time domain were calculated. The eye diagram calculated using the propagation constant extracted directly from the de-embedded S-parameters is also given as a reference.

The time domain data for measurement and the proposed two-term dielectric model using extracted $\tan\delta$ data are shown in Figs. 29 and 30. The corresponding frequency domain comparison is presented in Fig. 31. The results show good agreement in terms of the eye-opening and frequency-domain loss.

A similar comparison for the model using a one-term Djordjevic dielectric expression is shown in Fig. 32 for values of $\tan\delta$ picked at different frequencies (see Fig. 33). As can be seen, all examples exhibit a lack of accuracy either in time or frequency domain compared to the proposed two-term model.

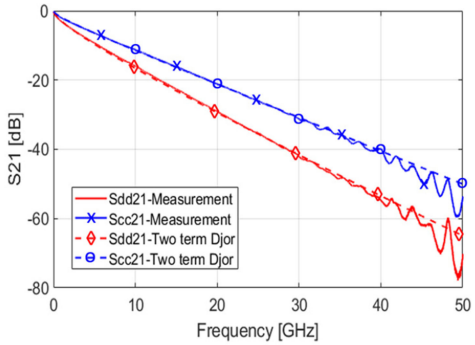

Fig. 31. Modeled insertion loss of the two-term Djordjevic model.

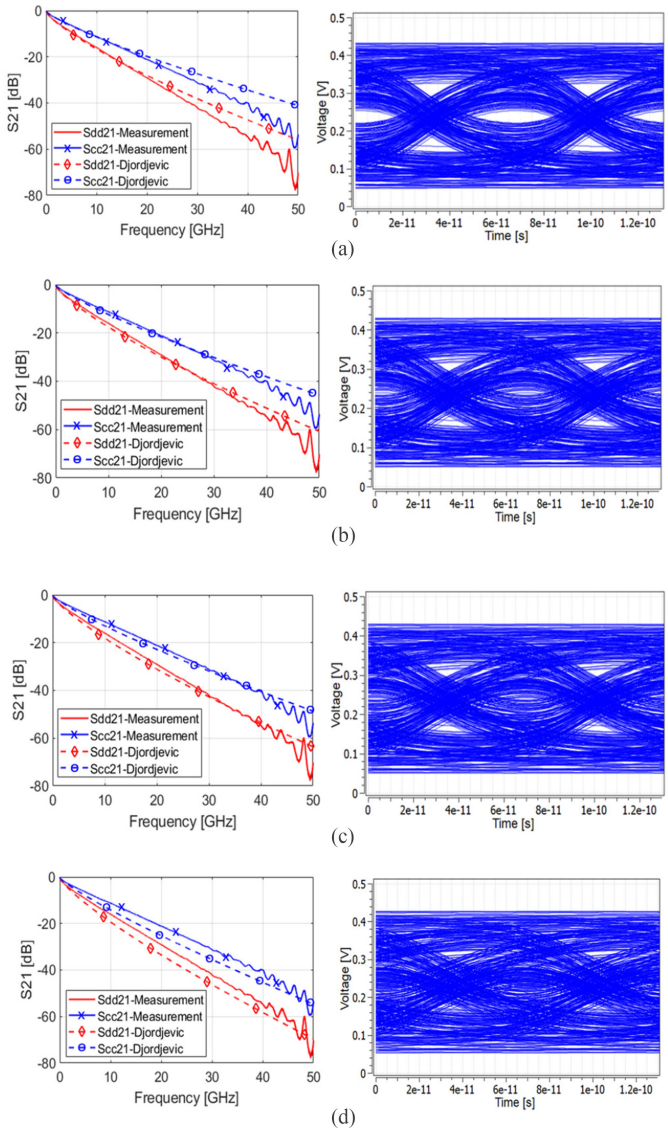

Fig. 32. Modeled insertion loss and eye diagram of the Djordjevic model with different $\tan\delta$ values. (a) One-term Djordjevic model using known $\tan\delta$ at 10 GHz ($\tan\delta = 0.0030$). (b) One-term Djordjevic model using known $\tan\delta$ at 20 GHz ($\tan\delta = 0.0038$). (c) One-term Djordjevic model using known $\tan\delta$ at 30 GHz ($\tan\delta = 0.0042$). (c) One-term Djordjevic model using known $\tan\delta$ at 30 Hz ($\tan\delta = 0.0042$). (d) One-term Djordjevic model using known $\tan\delta$ at 45 GHz ($\tan\delta = 0.0051$).

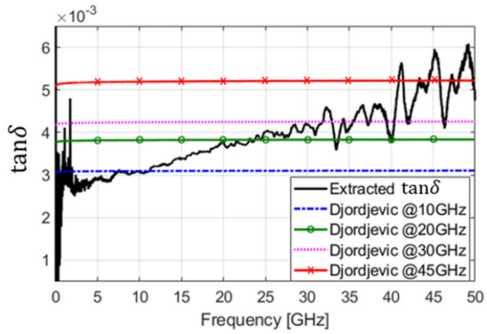

Fig. 33. One-term Djordjevic models generated by selecting $\tan\delta$ values at 10/20/30/45 GHz.

VII. Conclusion

A new $\tan\delta$ extraction method is proposed and analyzed. The method has low sensitivity to surface roughness, making extraction on low-loss materials possible (i.e., when the roughness contribution is comparable with the contribution of the dielectric loss). No *a priori* information about the behavior of the dielectric properties or attenuation constant is needed for extraction, which allows capturing arbitrary frequency-dependent behavior of the $\tan\delta$.

To estimate the accuracy of the extraction the error model taking into account errors due to de-embedding, VNA measurement and simulation is proposed. The error model explains inaccuracies in the extracted $\tan\delta$ at low at high frequency and allows to estimate impact of the measurement and simulation inaccuracies on the accuracy of extraction, which can be ultimately used to optimize the design of the extraction PCB.

To model the extracted frequency-dependent dielectric loss, a two-term Djordjevic model is proposed to fit the raw extraction result. Compared to the traditional one-term Djordjevic model, the proposed approach allows us to model the performance of signal-integrity simulation with improved accuracy using a small number of parameters.

References

[1] J. Krupka, D. Cros, M. Auburg, and P. Guillon, "Study of whispering-gallery modes in anisotropic single-crystal dielectric resonators," *IEEE Trans. Microw. Theory Techn.*, vol. 42, no. 1, pp. 56–61, Jan. 1994.

[2] J. Krupka, K. Derzakowski, A. Abramowicz, M. E. Tobar, and R. G. Geyer, "Use of whispering-gallery modes for complex permittivity determinations of ultra-low-loss dielectric materials," *IEEE Trans. Microw. Theory Techn.*, vol. 47, no. 6, pp. 752–759, Jun. 1999.

[3] J. Krupka, R. N. Clarke, O. C. Rochard, and A. P. Gregory, "Split post dielectric resonator technique for precise measurements of laminar dielectric specimens—Measurement uncertainties," in *Proc. 13th Int. Conf. Microw., Radar, Wireless*, 2000, vol. 1, pp. 305–308.

[4] X. Tian *et al.*, "Numerical investigation of glass-weave effects on high-speed interconnects in printed circuit board," in *Proc. IEEE Int. Symp. Electromagn. Compat.*, 2014, pp. 475–479.

[5] A. Koul, M. Y. Koledintseva, S. Hinaga, and J. L. Drewniak, "Differential extrapolation method for separating dielectric and rough conductor losses in printed circuit boards," *IEEE Trans. Electromagn. Compat.*, vol. 54, no. 2, pp. 421–433, Apr. 2012.

[6] S. Jin, X. Fang, B. Chen, H. Gao, X. Ye, and J. Fan, "Validating the transmission-line based material property extraction procedure including surface roughness for multilayer PCBs using simulations," in *Proc. IEEE Int. Symp. Electromagn. Compat.*, 2016, pp. 472–477.

[7] S. Jin, B. Chen, X. Fang, H. Gao, and J. Fan, "Improved 'root-omega' method for transmission-line based material property extraction for multilayer PCBs," *IEEE Trans. Electromagn. Compat.*, vol. 59, no. 4, pp. 1356–1367, Mar. 2017.
[8] M. Y. Koledinstseva, A. V. Rakov, A. I. Koledinstseva, J. L. Drewniak, and S. Hinaga, "Improved experiment-based technique to characterize dielectric properties of printed circuit boards," *IEEE Trans. Electromagn. Compat.*, vol. 56, no. 6, pp. 1559–1566, Dec. 2014
[9] M. Y. Koledinstseva, T. Vincent, A. Ciccomancini, and S. Hinaga, "Method of effective roughness dielectric in a PCB: Measurement and full-wave simulation verification," *IEEE Trans. Electromagn. Compat.*, vol. 57, no. 4, pp. 807–814, Aug. 2015.
[10] S. Yong *et al.*, "Dielectric dissipation factor (DF) extraction based on differential measurements and 2-D cross-sectional analysis," in *Proc. IEEE Int. Symp. Electromagn. Compat.*, 2018, pp. 217–222.
[11] A. R. Djordjevic, R. M. Biljic, V. D. Likar-Smiljanic, and T. K. Sarkar, "Wideband frequency-domain characterization of FR-4 and time-domain causality," *IEEE Trans. Electromag. Compat*, vol. 43, no. 4, pp. 662–667, Nov. 2001.
[12] X. Guo *et al.*, "Design methodology for behavioral surface roughness model," in *Proc. IEEE Int. Symp. Electromagn. Compat.*, 2016, pp. 927–931,
[13] S. Hall *et al.*, "Multigigahertz causal transmission line modeling methodology using a 3-D hemispherical surface roughness approach," *IEEE Trans. Microw. Theory Tech.*, vol. 55, no. 12, pp. 2614–2624, Dec. 2007.
[14] T. Granberg, *Handbook of Digital Techniques for High Speed Design*. Upper Saddle River, NJ, USA: Prentice Hall, 2004.
[15] C. R. Paul, *Analysis of Multiconductor Transmission Lines*, 2nd ed. Hoboken, NJ, USA: Wiley, 2008.
[16] D. M. Pozar, *Microwave Engineering*, 4th ed. Hoboken, NJ, USA: Wiley, 2012
[17] H. A. Wheeler, "Formulas for the skin effect," *Proc. IRE*, vol. 30, no. 9, pp. 412–424, Sep. 1942.
[18] M. E. Hellman and I. Palocz, "The effect of neighboring conductors on the currents and fields in plane parallel transmission lines," *IEEE Trans. Microw. Theory Techn.*, vol. 17, no. 5, pp. 254–259, May 1969.
[19] S. Yong, V. Khilkevich, X.-D. Cai, C. Sui, B. Sen, and J. Fan, "Comprehensive and practical way to look at far-end crosstalk for transmission lines with lossy conductor and dielectric," *IEEE Trans. Electromagn. Compat.*, to be published, doi: 10.1109/TEMC.2019.2902070.
[20] P. G. Huray *et al.*, "Fundamentals of a 3-D 'Snowball' model for surface roughness power losses," in *Proc. IEEE Conf. Signals Propag. Interconnects*, 2007, pp. 121–124.
[21] J. E. Bracken, "A causal huray model for surface roughness," *DesignCon*, Santa Clara, CA, USA, 2012.
[22] S. Hall and H. Heck, *Advanced Signal Integrity for High-Speed Digital Designs*. Hoboken, NY, USA: Wiley-IEEE Press, 2009.
[23] B. Chen, X. Ye, B. Samaras, and J. Fan, "A novel de-embedding method suitable for transmission-line measurement," in *Proc. IEEE Asia-Pac. Symp. Electromagn. Compat.*, 2015, pp. 1–4.
[24] Q. Huang, J. Li, J. Zhou, W. Wu, Y. Qi, and J. Fan, "De-embedding method to accurately measure high-frequency impedance of an O-shape spring contact," in *Proc. Int. Symp. IEEE Electromagn. Compat.*, 2014, pp. 600–603.
[25] B. Chen *et al.*, "Analytical and numerical sensitivity analyses of fixtures de-embedding," in *Proc. Int. Symp. IEEE Electromagn. Compat.*, 2016, pp. 440–444.
[26] B. Chen, J. He, Y. Guo, S. Pan, X. Ye, and J. Fan, "Multi-ports (2^n) $2\times$-thru de-embedding: Theory, validation, and mode conversion characterization," *IEEE Trans. Electromagn. Compat.*, vol. 61, no. 4, pp.1261–1270, Aug. 2019.
[27] G. Brist, "Design optimization of single-ended and differential impedance PCB transmission lines." [Online]. Available: https://www.jlab.org/eng/eecad/pdf/053designop.pdf. Accessed on: Oct. 2019.
[28] S. De, A. Gafarov, M. Y. Koledintseva, R. J. Stanley, J. L. Drewniak, and S. Hinaga, "Semi-automatic copper foil surface roughness detection from PCB microsection images," in *Proc. Int. Symp. IEEE Electromagn.Compat*, 2012, pp. 132–137.
[29] M. M. Ilic´, A. Ž Ilic, and B. M. Notaros, "Efficient large-domain 2-D FEM solution of arbitrary waveguides using p-refinement on generalized quadrilaterals," *IEEE Trans. Microw. Theory Tech.*, vol. 53, no. 4, pp. 1377–1383, Apr. 2005.
[30] S. Yong *et al.*, "A practical de-embedding error analysis method based on statistical circuit models of fixtures," in *Proc. Int. Symp. IEEE Electromagn. Compat*, 2019, pp. 45–50.
[31] "Keysight 2-port and 4-port PNA-X network analyze." [Online]. Available:http://literature.cdn.keysight.com/litweb/pdf/N5245-90008.pdf. Accessed on: Oct. 2019.
[32] J. Zhang *et al.*, "Causal RLGC(f) models for transmission lines from measured S-parameters," *IEEE Trans. Electromagn. Compat.*, vol. 52, no. 1, pp. 189–198, Feb. 2010.

Shaohui Yong (S'17) received the B.S. degree in electrical engineering from Beijing Jiaotong University, Beijing, China, in 2013, and the M.S. degree in electrical engineering, in 2015, from the Missouri University of Science and Technology (formlerly University of Missouri - Rolla), Rolla, MO, USA, where he is currently working toward the Ph.D. degree in electrical engineering at EMC Laboratory.

His reasearch interests include signal integrity in high-speed digital systems, electromagnetic interference, EMC measurement methods.

Victor Khilkevich (M'08) received the Ph.D. degree in electrical engineering from Moscow Power Engineering Institute, Technical University, Moscow, Russia, in 2001.

He is currently an Assistant Professor with the Missouri University of Science and Technology, Rolla, MO, USA. His research interests include microwave imaging, automotive electromagnetic compatibility modeling, and high-frequency measurement techniques.

Yuanzhuo Liu (S'19) received the B.E. degree in electrical and computer engineering from the Huazhong University of Science and Technology, Wuhan, China, in 2017. She is currently working toward the M.S. degree in electrical engineering from the EMC Laboratory, Missouri University of Science and Technology (formerly University of Missouri-Rolla), Rolla, MO, USA.

Her research interests include electromagnetic interference, signal integrity in high-speed digital systems, and microwave imaging.

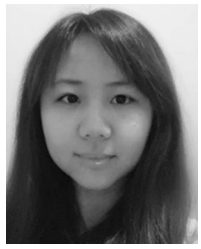

Han Gao (S'16) received the M.S. degree in electric engineering with the Electromagnetic Compatibility Laboratory, Missouri University of Science and Technology (University of Missouri—Rolla), Rolla, MO, USA, in 2019.

She is currently a Signal Integrity Engineer with the Cisco, San Jose, CA, USA. Her research interests include in both ASIC and surface roughness modeling in PCB, SerDes characterization, power integrity and PCB level, and generic differential transmission line modeling.

Scott Hinaga received the B.S. degree in chemistry from Stanford University, Stanford, CA, USA, in 1985.

He has been working with Cisco, San Jose, CA, USA, for ten years, with 20 years prior experience in PCB manufacturing engineering management. He is a Staff Manufacturing Engineer with the PCB Technology Group. His main projects have involved research and qualification of high-speed/low-loss PCB laminates, foil and glass, as well as characterization of conductor surface roughness effects on insertion loss.

Soumya De (S'07–M'13) received the B.E. degree in electronics engineering from Nagpur University, Maharashtra, India, in 2007, and the M.S. and Ph.D. degrees in electrical engineering from the Missouri University of Science and Technology (formerly the University of Missouri–Rolla), Rolla, MO, USA, in 2008 and 2012, respectively.

From 2012 to 2018, he was a Signal Integrity Engineer with Cisco, San Jose, CA, USA, and from 2018 to 2019, he was a EMC Design Engineer with Apple, Cupertino, CA, USA. He is currently a Hardware Engineer with Cruise in San Francisco, CA, USA. His current research interests include signal integrity, power integrity, electrostatic discharge, and electromagnetic compatibility for high-speed designs.

Darja Padilla received the Ph.D. degree in electrical engineering from the University of Colorado, Boulder, CO, USA, with concentration in optics and electromagnetics.

She is currently a Technical Leader with Cisco Systems, San Jose, CA, USA. Her main projects involve high-speed board and ASIC package design and advanced material characterization.

Douglas Yanagawa, received the M.S. degree in electrical engineering from Santa Clara University, Santa Clara, CA, USA, in 1990.

He was a Microprocessor Package Designer with MIPS Computer Systems and a Signal Integrity Engineer with Silicon Graphics. He has been with Cisco Systems as a Signal Integrity Engineer since 1998.

James Drewniak (S'85–M'90–SM'01–F'06) received the B.S., M.S., and Ph.D. degrees in electrical engineering from the University of Illinois at Urbana–Champaign, Champaign, IL, USA, in 1985, 1987, and 1991, respectively.

He is currently with the Electromagnetic Compatibility Laboratory, Department of Electrical and Computer Engineering, Missouri University of Science and Technology, Rolla, MO, USA. His research interests include electromagnetic compatibility, signal and power integrity, and electronic packaging.